PHYSICAL REVIEW B **91**, 125302 (2015)

Coherent transport and manipulation of spins in indirect-exciton nanostructures

A. Violante,[*] R. Hey, and P. V. Santos
Paul-Drude-Institut für Festkörperelektronik, Hausvogteiplatz 5-7, 10117 Berlin, Germany

(Received 19 August 2014; revised manuscript received 5 November 2014; published 5 March 2015)

We report on the coherent control and transport of indirect-exciton (*IX*) spins in GaAs double quantum well (DQW) nanostructures. The spin dynamics was investigated by optically generating spins using a focused, circularly polarized light spot and by probing their spatial distribution using spatially and polarization resolved photoluminescence spectroscopy. Optically injected *IX* spins precess while moving over distances exceeding 20 μm from the excitation spot with a precession length that depends on the spin transport direction as well as on the bias applied across the DQW structure. This behavior is attributed to the spin precession in the effective magnetic field induced by the spin-orbit interaction. From the dependence of the spin dynamics on the transport direction, bias, and external magnetic fields we directly determined the Dresselhaus and Rashba electron spin splitting coefficients for the DQW structure. The precession dynamics is essentially independent of the *IX* density, thus indicating that the long spin lifetimes are not associated with *IX* collective effects. The long *IX* lifetimes, together with the negligible contribution of holes to the spin dynamics, are rather attributed to spatial separation of the electron and hole wave functions by the electric field, which reduces the electron-hole exchange interaction. If extended to the single-exciton regime, the present results on coherent spin precession over long transport distances as well as the control of the spin vector using electric and magnetic fields open the way for the application of *IX* spins in quantum information processing.

DOI: 10.1103/PhysRevB.91.125302 PACS number(s): 71.35.−y, 75.76.+j, 75.70.Tj, 73.21.Fg

I. INTRODUCTION

An indirect (or dipolar) exciton (*IX*) consists of a Coulomb-correlated electron-hole pair with the individual particles confined in two closely spaced quantum wells (QWs) in a double quantum well (DQW) structure (cf. Fig. 1) subjected to a transverse electric field F_z. F_z controls via the quantum confined Stark effect both the *IX* energy and radiative lifetime, which can reach the μs range [1]. The electric field can be used to laterally confine *IX* gases in the DQW plane using electrostatic gates [2] as well as to control the interconversion between *IX*s and photons. In addition, the electrical dipoles arising from the charge separation give rise to strong repulsive exciton-exciton interactions [3]. Finally, *IX*s are composite bosons and, therefore, susceptible to the formation of collective phases, as evidenced by the experiments presented in Refs. [4–6]. These interesting *IX* properties have been combined to demonstrate different device functionalities including light storage cells, switches, and transistors [7–9]. The long *IX* lifetimes also enable the long-range transport and coupling of *IX* packets. Different approaches have also been introduced for the transport of *IX*s based on bare diffusion [10], drift induced by repulsive *IX-IX* interactions [4], or by using spatially varying electric fields, including electrostatic ramps [11] as well as moving electrostatic [12] and acoustic lattices [13–15].

Recently, the confinement of single *IX*s has been demonstrated [2], thus opening the way for applications of single *IX*s in quantum information processing [16]. Here, the manipulation and transport of *IX* spins offers further exciting perspectives. *IX*s have several favorable properties for spin control and manipulation. In particular, the reduced overlap between the electron and hole wave functions reduces not only the radiative lifetime but also the exchange interaction between the exciton-bound electron spins and the short-living hole spins (the excitonic or Bir-Aronov-Pikus (BAP) dephasing mechanism [17,18]), thus enhancing the *IX* spin lifetime [19–21].

The long lifetime also enables spin control using spin-orbit (SO) coupling. Due to the bulk inversion asymmetry (BIA) intrinsic to noncentrosymmetric III-V materials (such as GaAs) [22,23], moving spins feel an effective magnetic field (the Dresselhaus field [24], $\mathbf{B}_D$), which induces spin precession. In addition, the structural inversion asymmetry (SIA) created by F_z induces a tunable contribution to the SO magnetic field (the Rashba field [25], $\mathbf{B}_R$). F_z thus provides a powerful tool for electrical spin control during motion by modulating the total SO field $\mathbf{B}_{\mathrm{SO}} = \mathbf{B}_D + \mathbf{B}_R$ [26].

The SO fields can, however, also lead to the dephasing of exciton spin ensembles via the D'yakonov-Perel' dephasing mechanism. Finally, F_z also affects spins by changing the g factor [27].

The *IX* spin lifetime is also enhanced under high particle densities. In analogy with the spin dynamics of atomic condensates [28], the latter has been attributed to the formation of collective *IX* phases [20]. In particular, experiments carried out in this regime have lead to the observation of spin currents in *IX* gases with a variety of spatially resolved polarization patterns [29,30], which have been attributed to the SO magnetic field.

Most of the previous *IX* spin studies have addressed the spin dynamics very close to the spin excitation area (i.e., within distances <10 μm) [31], one exception being the self-organized extended (i.e., >20 μm) spin patterns reported for the collective regime at high *IX* densities [5]. In this work, we demonstrate that optically injected *IX* spins can be transported over distances exceeding 20 μm from the injection spot. These long transport distances arise from the fact that the *IX* motion is propelled by a radial effective force resulting from repulsive interactions in the region of high *IX* density close to

---

[*] violante@pdi-berlin.de

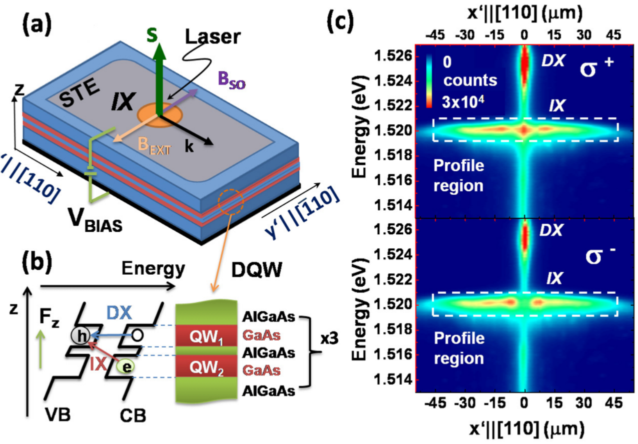

FIG. 1. (Color online) (a) Double quantum well (DQW) structures for indirect-exciton (*IX*) spin transport. The *IX*s are optically excited using a focused cw laser excitation in a DQW subject to an electric field (F_z) induced by a bias V_{bias} applied between the doped substrate and a semitransparent top electrode (STE). *IX* spin transport is mapped by imaging the *IX* photoluminescence (PL) emitted along direction k with polarization sensitivity. During motion along k, the spins precess under the spin-orbit ($\mathbf{B}_{\text{SO}}$) and external magnetic field ($\mathbf{B}_{\text{ext}}$). (b) Energy band diagram of the GaAs/(Al,Ga)As DQW along the vertical (z) direction showing the direct (*DX*) and *IX* transitions under the electric field F_z. (c) Spatially and spectrally resolved images of the PL with right (σ^+, upper panel) and left (σ^-, lower panel) circular polarizations recorded under a bias $V_{\text{bias}} = -2$ V and a laser power of 13 μW. *DX* and *IX* denote the emission from direct and indirect excitons in the DQW structure. The broad background close to the excitation point arises from excitons in the GaAs substrate.

the generation spot [10]. The spins coherently precess during motion: the precession length depends on the motion direction and can be controlled by the vertical field F_z applied across the DQW. This precession behavior, which does not depend on *IX* density, is attributed to the action of the anisotropic SO field on electron spins. From the dependence of the spin polarization on F_z, motion direction, and external magnetic field $\mathbf{B}_{\text{ext}}$, we have determined the *IX* spin lifetime as well as the absolute magnitude and orientation of the Dresselhaus and Rashba SO fields in the DQW structures. In contrast to the spin patterns in collective regimes addressed in Ref. [5], we show that the transport and manipulation of *IX* ensembles reported here takes place in the drift-diffusive regime, where the *IX*s suffer scattering events while moving preferentially along the radial direction. Although the long *IX* transport distances reported here result from particle-particle interactions, the spin dynamics reported here is not related to collective effects and should thus apply down to the single *IX* spin level.

In the following, we first describe the sample structure and the photoluminescence (PL) technique used to probe the transport of exciton spins. We then present experimental results demonstrating the transport and coherent precession of *IX* spins in the SO field together with detailed studies of the spin dynamics as a function of propagation direction, bias, and external magnetic fields. These results on spin transport are then analyzed and compared to previously published reports on SO effects on electron spins.

II. EXPERIMENTAL DETAILS

The samples used in the experiment contain three sets of asymmetric GaAs DQWs grown by molecular beam epitaxy on an n^+-doped GaAs(001) substrate [cf. Figs. 1(a) and 1(b)]. Each DQW is formed by a $d_{\text{QW}_1} = 14$ nm (QW$_1$) and a $d_{\text{QW}_2} = 17$ nm thick QW (QW$_2$) separated by a thin (4 nm thick) Al$_{0.3}$Ga$_{0.7}$As barrier. Multiple DQWs were used in order to enhance the photon yield of the PL experiments. The different QW widths enable the selective generation of direct excitons in either QW$_1$ or QW$_2$ by the appropriate selection of the excitation wavelength [32]. The electric field F_z for the formation of *IX*s was induced by a bias voltage V_{bias} applied between the n-doped substrate and a thin (10 nm thick) semitransparent Ti electrode (STE) deposited on the sample surface.

The spectroscopic experiments were carried out in a He bath cryostat at 2 K. Excitons were generated using a right circularly polarized beam from a cw Ti:sapphire laser resonant with the electron–heavy hole direct-exciton (*DX*) transition of the wider (QW$_2$) QW. The laser was focused onto a spot with a diameter of 2.5 μm using a microscope objective. The PL around the laser spot was collected by the same objective, analyzed regarding the circular polarization, and then imaged on the entrance slit of a spectrometer connected to a cooled charge-coupled-device (CCD) camera. The detected CCD images contain information about the energy (direction perpendicular to the slit) and spatial distribution (along the slit) of the PL intensity. The spatial (coordinate r) dependence of the spin polarization was calculated according to $\rho_z(r) = [I_{\sigma^+}(r) - I_{\sigma^-}(r)]/[I_{\sigma^+}(r) + I_{\sigma^-}(r)]$, where $I_{\sigma^+}(r)$ [$I_{\sigma^-}(r)$] denote the PL intensity at r with right (left) circular polarization.

III. RESULTS

A. Coherent spin precession during transport

Figure 1(c) compares PL images with right (σ^+) and left (σ^-) polarization recorded with the spectrometer slit aligned with the sample crystallographic direction $x' = [110]$. The emission patterns at 1.515 eV arises from the low-energy tail of *DX*s in QW$_2$. The spectrally broad PL background arises from excitons in the GaAs substrate.

In both cases, the emission is restricted to a region close to the excitation spot, thus indicating negligible diffusion distances for *DX*s. The line at 1.520 eV is associated with the emission of *IX*s in the DQW structure, which in this case was subject to a bias $V_{\text{bias}} = -2$ V. The emission extends to radii exceeding 40 μm; these long transport distances arise from the fact that the *IX*s are driven not only by diffusion but also by the drift forces induced by repulsive exciton-exciton dipolar interactions at the areas of high *IX* density close to the excitation area. This assertion is supported by the strong dependence of the extension of the *IX* PL cloud on the excitation density P_l, as displayed by the dashed and dash-dotted lines in Fig. 2(a). These curves display the spatial dependence of the total PL intensity (i.e., [$I_{\sigma^+}(r) + I_{\sigma^-}(r)$] determined from PL images for laser excitation powers of $P_l = 13$ μW [as in Fig. 1(c)] and 1.6 μW, respectively. The characteristic shape of the spatial PL profiles is consistent

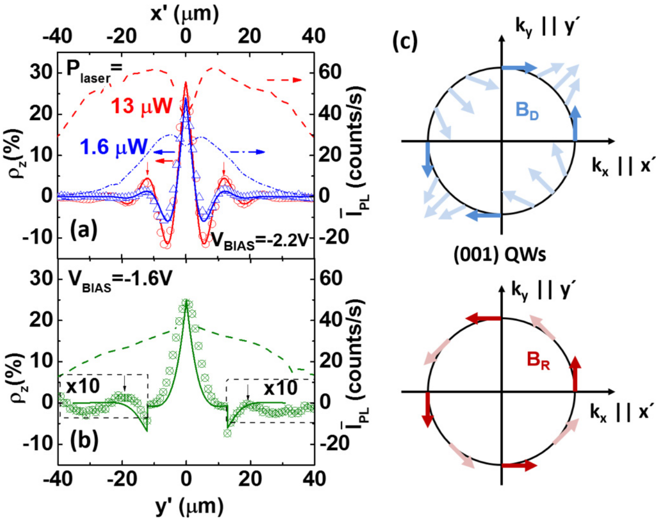

FIG. 2. (Color online) (a) Profiles for the spin polarization (ρ_z, symbols) and for the average PL intensity ($\bar{I}_{PL}$, dashed and dot-dashed lines) for *IX* transport along the $x'||[110]$ (symbols) recorded for laser excitation densities $P_\ell = 1.6\ \mu$W (open blue triangles) and 13 μW (open red circles). (b) Corresponding profiles for transport along $y'||[\bar{1}10]$ recorded for $P_\ell = 6\ \mu$W (green crossed circles). The solid lines superimposed on the symbols are fits of the experimental results to Eq. (1). (c) In-plane dependence of the Dresselhaus ($\mathbf{B}_D$) and Rashba ($\mathbf{B}_R$) contributions to the SO effective magnetic field $\mathbf{B}_{\mathrm{SO}} = \mathbf{B}_D + \mathbf{B}_R$.

with the observations of Ref. [4], which reported that the *IX* PL is reduced in the area of hot *IX*s close to the excitation spot. Furthermore, a closer look at Fig. 1(c) also reveals that the *IX* emission energy is redshifted as one moves away from the excitation spot. In fact, the average *IX* emission energy at $x' = 0\ \mu$m is ~0.5 meV higher than at $x' = 75\ \mu$m. This energetic blueshift is attributed to the strong repulsive *IX-IX* interactions at the high *IX* densities (estimated [33] to be of 2×10^{10} cm^{-2}) close to $x' = 0$.

The intensity of the circularly polarized *IX* emission in Fig. 1(c) is also spatially modulated with the maxima for the σ^+ polarization corresponding to minima in the σ^- polarization. The symbols in Fig. 2(a) display the corresponding profiles for the spin polarization ρ_z. This spatial PL modulation is attributed to the precession of the *IX* electron spins in the effective SO magnetic field B_{SO} during their motion away from the excitation spot. The ρ_z oscillations extend over a range of radial distances shorter than the radius of the emission cloud. While the amplitude of the oscillations increases with P_l, their spatial period remains essentially constant. An increase in spin polarization with excitation density was previously reported in Ref. [20] and attributed to the onset of collective *IX* effects. In our case, however, the precession length does not change with the excitation density, thus indicating that it does not depend on the *IX* density. The larger ρ_z amplitudes at high P_l are attributed to the shorter expansion times of the *IX* cloud, as a result of the reduced impact of the spin scattering processes.

As will be justified below, the oscillations in ρ_z are associated with the precession of the *IX* electron spin around the SO field $\mathbf{B}_{\mathrm{SO}}(\mathbf{k})$. In a nondegenerate QW at low temperatures (i.e., for thermal energies less than the QW confinement energy), the field $\mathbf{B}_{\mathrm{SO}}(\mathbf{k})$ acting on electron spins as well as the spin precession rate $\bar{\Omega}_{\mathrm{SO}}(\mathbf{k}) = \frac{g\mu_B B_{\mathrm{SO}}(\mathbf{k})}{\hbar}$ become proportional to the electron wave vector $\mathbf{k}$. In the ballistic transport regime, the spin precession length (for $\mathbf{B}_{\mathrm{ext}} = 0$) $\ell_p = \ell_{\mathrm{SO}} = \frac{\hbar k}{m_e} \frac{2\pi}{\Omega_{\mathrm{SO}}(\mathbf{k})}$ only depends on motion direction $\hat{\mathbf{k}} = \mathbf{k}/k$ (and not on the magnitude k of the wave vector). In the previous expression for ℓ_p, the effective velocity has been expressed as the ratio between the momentum $\hbar k$ and the electron mass m_e.

In the present experiments, the strong repulsive *IX-IX* interactions around the laser spot force the particles to move preferentially along the radial direction. During their drift-diffusive motion, the particles suffer scattering events. The resulting random fluctuations in momentum induce spin relaxation via the D'yakonov Perel' mechanism [34], which leads to a decay of ρ_z with the distance from the excitation spot. The characteristic spin decay length ℓ_s depends on the temporal dynamics of the carrier motion as well as on the details of the spin scattering processes. The larger ρ_z amplitudes at high P_l in Fig. 2(a) are attributed to the shorter expansion times of the *IX* cloud, which reduces the impact of the spin scattering processes. The effective precession length, in contrast, remains essentially the same as for ballistic transport.

The solid lines in Fig. 2(a) are fits of the experimental results to the damped oscillations expected from the previous model with a spatial dependence given by

$$\rho_z(\mathbf{r}) = \rho_z(0)e^{-r/\ell_s}\cos\left[2\pi r/\ell_p(\hat{\mathbf{r}})\right], \tag{1}$$

where $\hat{r}$ is the unit vector along the motion direction.

The fits were carried out with a single value for ℓ_p (i.e., independent of r). They yield $\ell_s = 5.7 \pm 0.7\ \mu$m and reproduce very well the measured spin polarization profiles (see also the Supplemental Material [35]).

B. Dependence on propagation direction

The wave vector ($\mathbf{k}$) dependence of the SO contributions $\mathbf{B}_D(\mathbf{k})$ and $\mathbf{B}_R(\mathbf{k})$ for a III-V QW is illustrated in Fig. 2(c). Here, we use a reference frame defined by the axes $x'||[110]$, $y'||[\bar{1}10]$, and $z||[001]$. The associated (temporal) electron spin precession frequencies Ω_i ($i = D,R$) can be written as a function of the wave vector $\mathbf{k}$ as [36]

$$\hbar\Omega_D(\mathbf{k}) = \gamma\left(\frac{\pi}{d_{\mathrm{QW}}^{\mathrm{eff}}}\right)^2 \begin{bmatrix} k_{y'} \\ k_{x'} \\ 0 \end{bmatrix}, \tag{2}$$

$$\hbar\Omega_R(\mathbf{k}) = 2F_z r_{41} \begin{bmatrix} k_{y'} \\ -k_{x'} \\ 0 \end{bmatrix}, \tag{3}$$

where γ and r_{41} are the Dresselhaus and Rashba spin constants, respectively. Equations (2) and (3) apply for small wave vectors, i.e., $|k'_x|,|k'_x| \ll \frac{\pi}{d_{\mathrm{QW}}^{\mathrm{eff}}}$. $d_{\mathrm{QW}}^{\mathrm{eff}}$ is the effective extension along z of the electronic wave function in the QW confining the electrons (QW$_2$ in the present case, as established by the sign of V_{bias}). $d_{\mathrm{QW}}^{\mathrm{eff}}$ is determined by both the QW width and by the penetration depth into the barrier layers. The corresponding amplitudes of the inverse precession lengths $\ell_{\mathrm{SO},i}^{-1}$ can be derived from the precession distance required for a spin rotation by 2π. The following expressions are obtained [37]:

$$\ell_{\mathrm{SO},D}^{-1} = \gamma \frac{m_e}{2\pi\hbar^2}\left(\frac{\pi}{d_{\mathrm{QW}}^{\mathrm{eff}}}\right)^2, \quad \ell_{\mathrm{SO},R}^{-1} = \pm\frac{m_e}{\pi\hbar^2} r_{41} F_z, \qquad (4)$$

where the $-$ $(+)$ sign applies for transport along the [110] ([$\bar{1}$10]) direction. If $\mathbf{B}_D || \mathbf{B}_R$ the resulting inverse precession length will be given by $\ell_{\mathrm{SO}}^{-1} = |\ell_{\mathrm{SO},D}^{-1} \pm \ell_{\mathrm{SO},R}^{-1}|$, where the sign is defined by the relative orientation of the two fields.

Equations (2), (3), and (4) predict that the precession length ℓ_{SO} depends both on the transport direction and bias electric field F_z. In order to check the in-plane anisotropy of $\mathbf{B}_{\mathrm{SO}}$, we show in Fig. 2(b) spin polarization profiles recorded for *IX* motion along the [$\bar{1}$10] surface direction [i.e., orthogonal to the one in Figs. 1(c) and 2(b)]. The precession length for this direction is much larger than for motion along the [110] direction [cf. Fig. 2(a)]. The larger precession length, which in this case becomes comparable with the spin decay length ℓ_s, makes the amplitude of the oscillations much weaker than in Fig. 2(a). The dependence of ℓ_{SO} on transport direction is in agreement with the diagrams of Fig. 2(c): while $\mathbf{B}_D$ and $\mathbf{B}_R$ are added for motion along [110], they partially cancel each other for motion along [$\bar{1}$10], thus implying a weaker SO field.

Interestingly, while on one hand a weaker $\mathbf{B}_{\mathrm{SO}}$ would reduce spin scattering, the visibility of the ρ_z oscillations would not be improved unless the constraint $\ell_{\mathrm{SO}} < \ell_s$ remains satisfied. On the other hand, a stronger $\mathbf{B}_{\mathrm{SO}}$ would lead to a shorter ℓ_{SO}. In this case, however, one would also need to reduce the size of the excitation spot to less than $\sim\ell_{\mathrm{SO}}/2$ to ensure visibility. In this case, however, one needs to reduce the excitation spot to dimensions at least a factor of 2 smaller than the oscillation period in order to detect the oscillations.

C. Electric spin control

The electric control of the spin precession frequency is demonstrated by the series of profiles recorded for transport along [110] in Fig. 3(a). The amplitude F_z of the electric field was determined from the applied V_{bias} using the procedure described in Ref. [14]. The precession length ℓ_{SO} is reduced by over 15% with increasing F_z, thus indicating an enhancement of the Rashba field $\mathbf{B}_R$ as well as of the total SO field $\mathbf{B}_{\mathrm{SO}}$. Larger changes can in principle also be achieved by applying more negative biases across the DQWs. These, however, also reduce the PL yield and may lead to field-induced carrier leakage out of the DQW structure, thus hampering an efficient spin detection [38].

The spatial precession frequencies (ℓ_{SO}) for the different field amplitudes were obtained by fitting the experimental data in Fig. 3(a) to Eq. (1). Details about the fitting procedure, which yield spin decay lengths $\ell_s = 5.7 \pm 0.7$ μm over the whole field range, can be found in the Supplemental Material [35]. Values for inverse precession length ℓ_{SO}^{-1} are plotted as a function of the transverse electric field in Fig. 3(b). The solid line is a fit of the data measured along x' to the expression $\ell_{\mathrm{SO}}^{-1} = \ell_{\mathrm{SO},D}^{-1} + \ell_{\mathrm{SO},R}^{-1}$ [cf. Eq. (4)], which gives $\gamma = 17.9$ eV Å^3, $r_{41} = -8.5$ e Å^2, and $d_{\mathrm{QW}}^{\mathrm{eff}} = 21$ nm (the signs for γ and r_{41} will be determined below). The associated spatial precession frequencies $\ell_{\mathrm{SO},D}^{-1}$ and $\ell_{\mathrm{SO},R}^{-1}$ for propagation along x' are illustrated by the dashed lines. For negative biases, *IX*s are created in the DQW structure with the electrons confined within the QW$_2$. The value for $d_{\mathrm{QW}}^{\mathrm{eff}}$ used in the fits is compatible with an electronic wave function with a penetration depth of 2 nm in the barriers. As will be further discussed later, these SO parameters agree well with values reported in the literature.

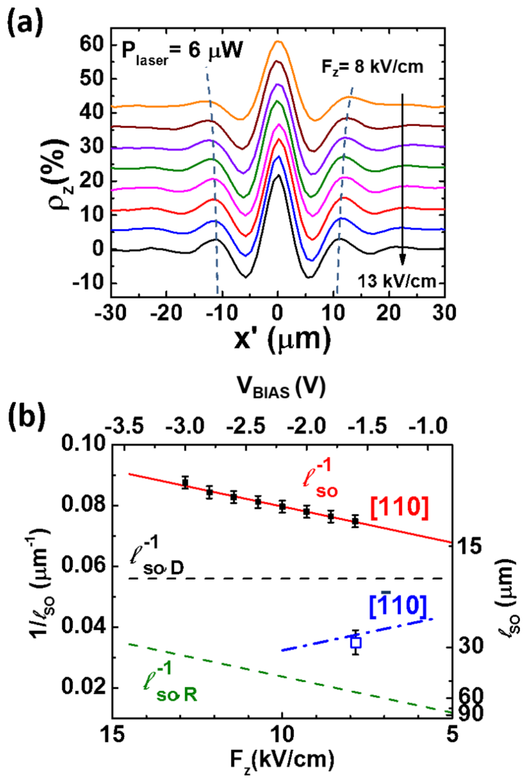

FIG. 3. (Color online) (a) Profiles for the polarization (ρ_z, solid lines) of spins moving along $x'||[110]$ recorded as a function of the electric field F_z applied along the growth direction of the DQW structure. (b) Dependence of the spin spatial precession frequency $1/\ell_{\mathrm{SO}}$ on the electric field F_z for transport along $x'||[110]$ (solid symbols) and $y'||[\bar{1}10]$ (open symbol). The upper scale displays the corresponding bias V_{bias} applied across the DQW structure. The solid line is a fit of the data along [110] to $\ell_{\mathrm{SO}}^{-1} = \ell_{\mathrm{SO},D}^{-1} + \ell_{\mathrm{SO},R}^{-1}$ [cf. Eq. (4)] with $\gamma = 17.9$ eV Å^3, $r_{41} = -8.5$ e Å^2, and $d_{\mathrm{QW}}^{\mathrm{eff}} = 21$ nm. The corresponding inverse precession lengths $\ell_{\mathrm{SO},D}^{-1}$ and $\ell_{\mathrm{SO},R}^{-1}$ are illustrated by the dashed lines. The dot-dashed line shows the expected spatial precession frequency for motion along [$\bar{1}$10].

The open symbol in Fig. 3(b) shows the inverse precession period measured for spin propagation along y', where the Dresselhaus contribution changes sign relative to the x' direction. The measured value agrees well with the calculated spatial precession frequencies ℓ_{SO}^{-1} for propagation along this direction (dash-dotted line). Note that the change in relative signs of the Rashba and Dresselhaus effective magnetic fields can, in principle, also be attained for a fixed motion direction by simply reversing the bias polarity. For the asymmetric DQWs used in the present experiments, however, a reversal in direction of F_z drives the electrons to the narrow QW, thus also changing the magnitude of the Dresselhaus contribution. In addition, while the leakage current is very low for negative

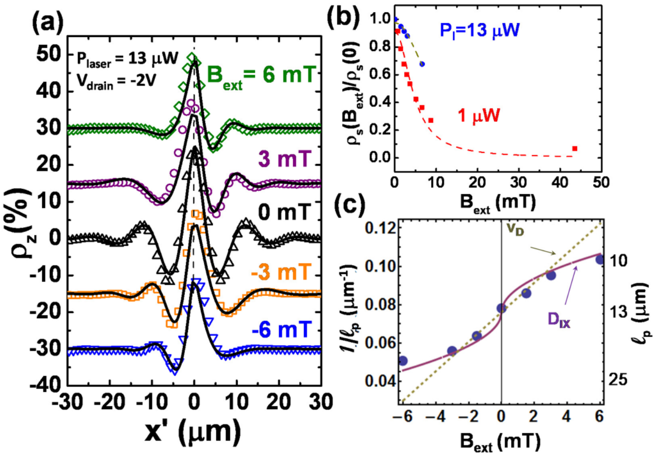

FIG. 4. (Color online) (a) Spin polarization profiles (open symbols) as a function of an external magnetic field ($\mathbf{B}_{\text{ext}}$). The curves are stacked for clarity. The solid lines are fits to the polarization profiles according to Eq. (1). (b) ρ_z close to the excitation spot as a function of $\mathbf{B}_{\text{ext}}$ measured for optical excitation densities $P_l = 13\ \mu$W (squares) and 1 μW (dots). The dashed lines display fits to Eq. (5), from which one extracts spin lifetimes of 6 and 3 ns, respectively. (c) Dependence of the inverse precession period ($1/\ell_p = 1/\ell_{\text{SO}} + 1/\ell_B$, where ℓ_{SO} and ℓ_B are the precession period around the SO and external fields, respectively) on $\mathbf{B}_{\text{ext}}$ (symbols). The lines are the predictions from the diffusion (D_{IX}) and drift (v_D) models discussed in the text.

biases (a few nA), it increases considerably for high positive biases.

D. Magnetic field dependence

An external magnetic field $\mathbf{B}_{\text{ext}}$ applied along the DQW plane provides an additional degree of freedom to control the spin vector. The experiments were carried out under the configuration illustrated in Fig. 1(a), where spins were mapped while moving along x' under an external field $\mathbf{B}_{\text{ext}}||y'$ and collinear with $\mathbf{B}_{\text{SO}}$. Figure 4(a) displays ρ_z profiles along x' recorded under different external magnetic fields. Large magnetic fields ($|\mathbf{B}_{\text{ext}}| > 6$ mT) mainly reduce the overall spin polarization via the Hanle effect, from which one can extract the spin dephasing time τ_s. For that purpose, we plot in Fig. 4(b) the *IX* spin polarization at the excitation spot $\bar\rho_z$ as a function of $\mathbf{B}_{\text{ext}}$. The lines superimposed on the data points are fits to the Hanle expression:

$$\bar\rho_z(B_{\text{ext}}) = \frac{\bar\rho_z(0)}{1+(\omega_L\tau^*)^2} \quad \text{with} \quad \hbar\omega_L = g_e\mu_B B_{\text{ext}}, \tag{5}$$

where $\frac{1}{\tau^*} = \frac{1}{\tau_{IX}} + \frac{1}{\tau_s}$ and τ_{IX} is the *IX* lifetime. By using the conduction band g factor $|g_e| = 0.44$ and considering $\tau_{IX} \gg \tau_s$, one extracts from the fits spin lifetimes of 6 and 3 ns for excitation powers of $P_l = 1\ \mu$W and 13 μW, respectively. These lifetimes are considerably longer than the typical carrier scattering times, thus confirming that the spin dynamics investigated here takes place in drift-diffusive rather than ballistic regime.

In contrast to strong magnetic fields, weak fields mainly affect the spin precession length, as indicated by the symbols in Fig. 4(c). The precession frequencies are extracted fitting the experimental data according to Eq. (1) [Fig. 4(a), solid lines]. The fits yield a spin decay length $\ell_{\text{SO}} = 5.5 \pm 0.6\ \mu$m over the whole field range. Furthermore, while the SO field reverses with carrier momentum, the external field has a fixed direction and its action on the spin vector only depends on time. These features can be exploited to determine the absolute orientation of $\mathbf{B}_{\text{SO}}$. When $\mathbf{B}_{\text{ext}}$ is oriented along $+y'$ [upper curves for $\mathbf{B}_{\text{ext}} > 0$ in Fig. 4(a)], the spatial spin precession rate increases (reduces) for spins moving along $+x'$ ($-x'$). The opposite behavior is observed when the orientation of $\mathbf{B}_{\text{ext}}$ reverses (curves for $\mathbf{B}_{\text{ext}} < 0$). From these results, together with the increase of the spatial precession frequency along the x' with $|F_z|$ [cf. Fig. 3(a)], we unambiguously establish that both the Rashba and Dresselhaus SO fields point towards y' when spins move along x'. The Dresselhaus splitting constant γ in Eq. (2) is thus positive while the Rashba parameter r_{41} is negative.

The different natures of the two fields also allow us to extract information about the precession dynamics during motion and their impact on the precession length ℓ_p. Here, we first note that the different ℓ_p values in Fig. 4(a) along $+x'$ and $-x'$ implies that both fields (i.e., $\mathbf{B}_{\text{SO}}$ and $\mathbf{B}_{\text{ext}}$) must act simultaneously on the spins during motion. This becomes clear if one considers the hypothetical situation, where the spins initially move to the final position x' within a very short time [thereby precessing only around $\mathbf{B}_{\text{SO}}(\mathbf{k})$] and then remain trapped there until recombination (thus precessing only around $\mathbf{B}_{\text{ext}}$). In this case, $\mathbf{B}_{\text{ext}}$ would simply add a fixed (i.e., position independent) phase to the spatial oscillations determined by $\mathbf{B}_{\text{SO}}$ and ℓ_p would be the same for spin motion along both the positive and negative x' axes, in contrast to the results displayed in Fig. 4(a).

Since $\mathbf{B}_{\text{ext}}$ and $\mathbf{B}_{\text{SO}}$ are collinear in Fig. 4(a), the spatial precession frequency can be written as $\ell_p^{-1} = \ell_{\text{SO}}^{-1} + \ell_B^{-1}(\mathbf{B}_{\text{ext}})$, where $\ell_B^{-1}(\mathbf{B}_{\text{ext}})$ is the contribution associated with the external field. In order to account for the dependence of ℓ_p^{-1} on $\mathbf{B}_{\text{ext}}$ one needs information about the spin position x' as a function of time (t). We consider in the following two extreme situations. First, if the motion is mainly driven by the *IX*-*IX* repulsion forces at the excitation region, the carriers are expected to move with an approximately constant velocity v_D, yielding $\ell_B^{-1}(B_{\text{ext}}) = \ell_{B,v_D}^{-1} = \frac{g\mu_B}{2\pi\hbar}\frac{\mathbf{B}_{\text{ext}}}{v_D}$. This model predicts the linear dependence of ℓ_p^{-1} on field indicated by the dashed line in Fig. 4(c). The small values used for $v_D = 800$ m/s, which corresponds to only ~10% of the average *IX* thermal velocity at 2 K, probably arise from the fact that diffusion has been completely neglected. While the behavior for small fields is well accounted for, the model fails to reproduce the deviations from linearity observed as the $|\mathbf{B}_{\text{ext}}|$ increases. The second extreme situation occurs if motion is purely driven by diffusion, in which case $x' \approx \sqrt{D_{IX}t}$, where D_{IX} is the *IX* diffusion coefficient and t the diffusion time. A straightforward calculation yields $\ell_B^{-1}(B_{\text{ext}}) = \ell_{B,D}^{-1} = \sqrt{\frac{g\mu_B}{2\pi\hbar}\frac{\mathbf{B}_{\text{ext}}}{D_{IX}}}$, leading to the behavior depicted by the solid line in Fig. 4(c). The calculations were carried out using an *IX* diffusion coefficient $D_{IX} = 400\ \text{cm}^2/\text{s}$, which is much larger than the one expected from Ref. [10] for diffusion in a 15 nm wide QW. Despite its simplicity, this approximation reproduces reasonably well the measured behavior for large field amplitudes. A good fit requires, however, values for D_{IX} much higher that those expected from Ref. [10]. These become necessary to reduce the *IX* transport (and precession) time and, in that way, compensate for the errors arising from neglecting drift effects. In order to better describe the data of Fig. 4(c) one needs a more elaborate model to account for the roles of diffusion and drift on the spin dynamics under an external magnetic field, which is out of the scope of the present paper.

IV. DISCUSSION

The experimental results of the previous section unambiguously show the coherent precession of optically excited spins in the effective magnetic field $\mathbf{B}_{\mathrm{SO}}$ induced by the SO interaction. The spin precession period depends on the in-plane motion direction it is essentially independent of the *IX* density and can be controlled by external electric and magnetic fields. The measured spin lifetimes (of a few ns) indicate that transport takes place in the drift-diffusive regime. The spin dynamics is well described by taking into account the SO parameters as well as the g factor for electrons in GaAs, thus showing that it is determined by the *IX* electron spins. In fact, the SO parameter $\gamma = 17.9$ eV Å^3 compares well with those determined from electron spin transport in (100) [39], (110) [40], and (111) QWs [38] with comparable widths. The magnitude of the Rashba parameter $r_{41} = -8.5$ e Å^2, however, lies above the experimental values of 4 and 6 ± 1 e Å^2 of Refs. [41] and [38], respectively, as well as the calculated value of 5.2 ± 1 e Å^2 from Ref. [37]. While further investigations are required to clarify this difference, we speculate that it may be related to the asymmetric composition profile of the DQW structure along the growth direction, which makes the electronic wave functions more susceptible to the applied electric field.

The coherent transport and precession of electron spins in the SO field in the drift-diffusive transport regime has been previously reported for bulk GaAs layers [42,43] as well as QW structures [39,40,42,44,45]. In these experiments, electron transport has been driven by an external electric (or piezoelectric field): in this way, the spins could be moved over microscopic distances before dephasing (assumed to be due to the D'yakonov-Perel' mechanism [34]) sets in. In the present case, the *IX*s' motion is propelled by *IX*-*IX* interaction forces, rather than an externally applied field. To our knowledge, the coherent precession of spins injected in an undoped QWs in the absence of an electric driving field demonstrated here has so far not been reported.

The observation of coherent spin precession in the SO field requires small ratios $\ell_{\mathrm{SO}}/\ell_s$ [cf. Eq. (1)]. Here, $\ell_{\mathrm{SO}} \sim a_{\mathrm{SO}}\langle\Omega_{\mathrm{SO}}\rangle$ (a_{SO} is a proportionality constant and the $\langle\,\rangle$'s denote thermal averages over the transport path) only depends on the strength of the SO interaction. The spin decay length l_s, in contrast, depends on transport time. For purely diffusive motion in the D'yakonov-Perel' regime, $l_s \sim \sqrt{\frac{D_{IX}}{t}\frac{1}{\tau_c\langle\Omega_{\mathrm{SO}}^2\rangle}}$, where τ_c is the carrier scattering time and D_{IX} the diffusion coefficient. As a result, the requirement $\ell_{\mathrm{SO}}/\ell_s \sim \frac{\tau_c}{\sqrt{D_{IX}}}\langle\Omega_{\mathrm{SO}}\rangle^3 a_{\mathrm{SO}}\sqrt{t} < 1$ becomes increasingly difficult to be satisfied for long transport times t (as well as for strong SO fields). In the present experiments, the expansion forces due to *IX*-*IX* repulsive interactions have a fundamental role: they considerably reduce the transport time, thus increasing ℓ_s and enabling the observation of precession oscillations before decoherence sets in.

Coherent spin patterns resulting from precession in the SO field have been reported for macroscopically ordered *IX* phases [5,29]. The long spin coherence lengths required for their formation have been attributed to the reduced scattering in the ordered state, which enables *IX* transport in the ballistic regime. The results presented in the previous section show that long spin lifetimes and transport lengths, as well as coherent precession in the SO field, can also be achieved in the drift-diffusive regime. This behavior occurs over a wide range of *IX* densities, thus indicating that it is not associated with collective effects. Interestingly, the spatial extent of the precession oscillations reported here is comparable to the ones for the self-organized spin patterns [29]. There are, however, fundamental differences between the two cases. While the spin pattern observed in Ref. [29] results from self-organization and does not rely on the initial *IX* polarization, the ones presented here appear as a consequence of the coherent transport of optically injected spins. In addition, the dynamics observed here is associated with electron spin precession, while Ref. [29] has invoked the simultaneous evolution of hole and electron spins.

Finally, as in most of the reports on the coherent precession of optically injected spins in the SO field, e.g., Refs. [39,40,44,45]), the absence of hole spin contributions to the spin dynamics is attributed to the short hole spin coherence times as well as the spatial separation of the electron and hole wave function in the DQW structure. Since we have excited and probed *IX* spins, an interesting question is whether the electrons and hole remain bound during transport. Although we cannot present conclusive evidence for this behavior, we mention that the *IX* spins have been excited with small excess energy (∼10 meV), thus reducing the probability of *IX* dissociation followed by the spatial separation of electrons and holes. In addition, the *IX* spatial profiles [cf., e.g., Fig. 1(c)] do not show the characteristic rings [4] observed when electrons and holes diffuse independently.

V. CONCLUSIONS

We have presented experimental evidence for the coherent precession of moving *IX* spins under the effective magnetic field induced by the SO interaction. The precession dynamics is essentially independent of the *IX* density, but can be controlled by an external bias (via changes in the SO field) or magnetic field. The spin dynamics is well explained by taking into account the precession of the *IX* electron spins in the SO field, with no noticeable hole spin contribution. The technique used by us allows for the control and discrimination of precession effects arising from the Rashba and Dresselhaus SO contributions, as well as those induced by an external magnetic field. In this way, we were able to directly determine the absolute value and sign of the spin splitting parameters for the Rashba and Dresselhaus SO mechanisms. In addition, the spin dynamics in the presence of an external magnetic field yield information about the precession dynamics during transport. The long spin transport distances as well as the control of the spin vector demonstrated here open the way for the use of *IX* spins to encode and manipulate quantum information in optoelectronic semiconductor devices.

ACKNOWLEDGMENTS

We thank Manfred Ramsteiner and Alberto Hernández-Mínguez for the useful discussions and comments on the manuscript. We are indebted to S. Rauwerdink, W. Seidel, S. Krauß, and A. Tahraoui for the assistance in the preparation of the samples. We also acknowledge financial support from the German DFG (Grant No. SA-598/9).

---

[1] K. Sivalertporn, L. Mouchliadis, A. L. Ivanov, R. Philp, and E. A. Muljarov, Phys. Rev. B **85**, 045207 (2012).

[2] G. J. Schinner, J. Repp, E. Schubert, A. K. Rai, D. Reuter, A. D. Wieck, A. O. Govorov, A. W. Holleitner, and J. P. Kotthaus, Phys. Rev. Lett. **110**, 127403 (2013).

[3] K. Cohen, R. Rapaport, and P. V. Santos, Phys. Rev. Lett. **106**, 126402 (2011).

[4] L. V. Butov, A. C. Gossard, and D. S. Chemla, Nature (London) **418**, 751 (2002).

[5] A. A. High, J. R. Leonard, A. T. Hammack, M. M. Fogler, L. V. Butov, A. V. Kavokin, K. L. Campman, and A. C. Gossard, Nature (London) **483**, 584 (2012).

[6] Y. Shilo, K. Cohen, B. Laikhtman, K. West, L. Pfeiffer, and R. Rapaport, Nat. Commun. **4**, 2335 (2013).

[7] A. A. High, E. E. Novitskaya, L. V. Butov, M. Hanson, and A. C. Gossard, Science **321**, 229 (2008).

[8] A. G. Winbow, A. T. Hammack, L. V. Butov, and A. C. Gossard, Nano Lett. **7**, 1349 (2007).

[9] G. Grosso, J. Graves, A. T. Hammack, A. High, L. V. Butov, M. Hanson, and A. C. Gossard, Nat. Photonics **3**, 577 (2009).

[10] Z. Vörös, R. Balili, D. W. Snoke, L. Pfeiffer, and K. West, Phys. Rev. Lett. **94**, 226401 (2005).

[11] A. Gärtner, A. W. Holleitner, J. P. Kotthaus, and D. Schuh, Appl. Phys. Lett. **89**, 052108 (2006).

[12] A. G. Winbow, J. R. Leonard, M. Remeika, Y. Y. Kuznetsova, A. A. High, A. T. Hammack, L. V. Butov, J. Wilkes, A. A. Guenther, A. L. Ivanov *et al.*, Phys. Rev. Lett. **106**, 196806 (2011).

[13] J. Rudolph, R. Hey, and P. V. Santos, Phys. Rev. Lett. **99**, 047602 (2007).

[14] S. Lazić, A. Violante, K. Cohen, R. Hey, R. Rapaport, and P. V. Santos, Phys. Rev. B **89**, 085313 (2014).

[15] A. Violante, K. Cohen, S. Lazić, R. Hey, R. Rapaport, and P. V. Santos, New J. Phys. **16**, 033035 (2014).

[16] I. Zutic, J. Fabian, and S. D. Sarma, Rev. Mod. Phys. **76**, 323 (2004).

[17] G. L. Bir, A. G. Aronov, and G. E. Pikus, Sov. Phys. JETP **42**, 705 (1975).

[18] G. L. Bir and G. E. Pikus, *Symmetry and Strain-Induced Effects in Semiconductors* (John Wiley & Sons, New York, 1974).

[19] A. Larionov, V. Timofeev, J. Hvam, and C. Soerensen, JETP Lett. **71**, 117 (2000).

[20] A. V. Larionov, V. E. Bisti, M. Bayer, J. Hvam, and K. Soerensen, Phys. Rev. B **73**, 235329 (2006).

[21] K. Kowalik-Seidl, X. P. Vögele, B. N. Rimpfl, S. Manus, J. P. Kotthaus, D. Schuh, W. Wegscheider, and A. W. Holleitner, Appl. Phys. Lett. **97**, 011104 (2010).

[22] M. I. D'yakonov and V. I. Perel', Sov. Phys. JETP **33**, 1053 (1971).

[23] M. I. Dyakonov, *Spin Physics in Semiconductors* (Springer, Berlin, 2008).

[24] G. Dresselhaus, Phys. Rev. **100**, 580 (1955).

[25] E. I. Rashba, Sov. Phys. Solid State **2**, 1109 (1960).

[26] A. V. Larionov and L. E. Golub, Phys. Rev. B **78**, 033302 (2008).

[27] M. Poggio, G. M. Steeves, R. C. Myers, N. P. Stern, A. C. Gossard, and D. D. Awschalom, Phys. Rev. B **70**, 121305(R) (2004).

[28] E. A. Burt, R. W. Ghrist, C. J. Myatt, M. J. Holland, E. A. Cornell, and C. E. Wieman, Phys. Rev. Lett. **79**, 337 (1997).

[29] A. A. High, A. T. Hammack, J. R. Leonard, S. Yang, L. V. Butov, T. Ostatnický, M. Vladimirova, A. V. Kavokin, T. C. H. Liew, K. L. Campman *et al.*, Phys. Rev. Lett. **110**, 246403 (2013).

[30] A. V. Kavokin, M. Vladimirova, B. Jouault, T. C. H. Liew, J. R. Leonard, and L. V. Butov, Phys. Rev. B **88**, 195309 (2013).

[31] J. R. Leonard, Y. Y. Kuznetsova, S. Yang, L. V. Butov, T. Ostatnick, A. Kavokin, and A. C. Gossard, Nano Lett. **9**, 4204 (2009).

[32] M. Stern, V. Garmider, E. Segre, M. Rappaport, V. Umansky, Y. Levinson, and I. Bar-Joseph, Phys. Rev. Lett. **101**, 257402 (2008).

[33] R. Zimmermann and C. Schindler, Solid State Commun. **144**, 395 (2007).

[34] M. I. D'yakonov and V. I. Perel', Sov. Phys. Solid State **13**, 3023 (1972).

[35] See Supplemental Material at http://link.aps.org/supplemental/10.1103/PhysRevB.91.125302 for details about the fitting procedure.

[36] A. Hernández-Mínguez, K. Biermann, R. Hey, and P. V. Santos, Phys. Status Solidi B **251**, 1736 (2014).

[37] R. Winkler, *Spin-Orbit Coupling Effects in Two-Dimensional Electron and Hole Systems* (Springer, Berlin, 2003).

[38] A. Hernández-Mínguez, K. Biermann, R. Hey, and P. Santos, Phys. Rev. Lett. **109**, 266602 (2012).

[39] J. A. H. Stotz, R. Hey, P. V. Santos, and K. H. Ploog, Nat. Mater. **4**, 585 (2005).

[40] O. D. D. Couto, Jr., F. Iikawa, J. Rudolph, R. Hey, and P. V. Santos, Phys. Rev. Lett. **98**, 036603 (2007).

[41] P. S. Eldridge, W. J. H. Leyland, P. G. Lagoudakis, R. T. Harley, R. T. Phillips, R. Winkler, M. Henini, and D. Taylor, Phys. Rev. B **82**, 045317 (2010).

[42] Y. Kato, R. C. Myers, A. C. Gossard, and D. D. Awschalom, Nature (London) **427**, 50 (2004).

[43] M. Beck, C. Metzner, S. Malzer, and G. H. Doehler, Europhys. Lett. **75**, 597 (2006).

[44] H. Sanada, T. Sogawa, H. Gotoh, K. Onomitsu, M. Kohda, J. Nitta, and P. V. Santos, Phys. Rev. Lett. **106**, 216602 (2011).

[45] H. Sanada, Y. Kunihashi, H. Gotoh, K. Onomitsu, M. Kohda, J. Nitta, P. V. Santos, and T. Sogawa, Nat. Phys. **9**, 280 (2013).